



# Calcium as an innovative and effective catalyst for the synthesis of graphene-like materials from cellulose

Théotime Beguerie, Elsa Weiss-Hortala, Ange Nzihou

## ► To cite this version:

Théotime Beguerie, Elsa Weiss-Hortala, Ange Nzihou. Calcium as an innovative and effective catalyst for the synthesis of graphene-like materials from cellulose. Scientific Reports, 2022, 12, pp.21492. 10.1038/s41598-022-25943-3 . hal-03918518

**HAL Id: hal-03918518**

**<https://imt-mines-albi.hal.science/hal-03918518>**

Submitted on 2 Jan 2023

**HAL** is a multi-disciplinary open access archive for the deposit and dissemination of scientific research documents, whether they are published or not. The documents may come from teaching and research institutions in France or abroad, or from public or private research centers.

L'archive ouverte pluridisciplinaire **HAL**, est destinée au dépôt et à la diffusion de documents scientifiques de niveau recherche, publiés ou non, émanant des établissements d'enseignement et de recherche français ou étrangers, des laboratoires publics ou privés.



Distributed under a Creative Commons Attribution 4.0 International License



OPEN

# Calcium as an innovative and effective catalyst for the synthesis of graphene-like materials from cellulose

Théotime Béguerie<sup>1</sup>, Elsa Weiss-Hortala<sup>1</sup> & Ange Nzihou<sup>1,2,3</sup>✉

Pyrolysis of lignocellulosic biomass (hard carbon) produces poorly graphitic biochar. In this study, nano-structured biochars were produced from microcrystalline cellulose using calcium as a non-conventional catalyst. Calcium is abundant, environmental-friendly and widely accessible. Graphitization of calcium-impregnated cellulose was carried out at 1800 °C, a temperature below 2000 °C where the graphitization usually occurs. XRD, Raman spectroscopy, high-resolution TEM together with the in-house numerical tool developed enable the quantification of the graphene fringes in the biochars. The non-impregnated cellulose biochar was composed of short and poorly stacked graphene fringes. The impregnation with 2 wt.% of calcium led to the conversion of the initial structure into a well-organized and less defective graphene-like one. The graphene-like structures obtained were composed of tens of stacked graphene fringes with a crystallite size up to 20 nm and an average interlayer spacing equal to 0.345 nm, close to the reference value of standard hexagonal graphite (0.3354 nm). The increase of the calcium concentration did not significantly improve the crystallite sizes of the graphene-like materials but rather drastically improved their rate. Our results propose a mechanism and provide new insights on the synthesis of graphene-like materials from bio-feedstocks using calcium where the literature is focused on transition metals such as iron and nickel among others. The decrease of the graphitization temperature below 2000 °C should lower the production cost as well as the environmental impact of the thermal graphene-like materials synthesis using biomass. This finding should stimulate further research in the field and broaden the application perspectives.

Graphene is a bidimensional carbon material with one atomic layer as thickness<sup>1</sup>. Graphene sheets are precursors to carbon nanotubes, fullerene, carbon fibers, carbon black or graphite<sup>2–4</sup>. Depending on the characteristics such as the length and the orientation of the graphene sheets, various properties could be developed among which, the electrical conductivity, the mechanical or thermal resistance<sup>5,6</sup>. Therefore, graphene is considered as a high-performance material, promising for a wide range of applications such as batteries, energy storage, electronics, and biology<sup>4,7–11</sup>.

Nowadays, graphene can be produced from fossil feedstocks by either top-down or bottom-up processes<sup>3,12–16</sup>. Top-down processes include mechanical or chemical exfoliation of extracted graphite to isolate the graphene sheets. Bottom-up processes involve the synthesis of graphene from gaseous hydrocarbon precursors. The advantages and drawbacks of each process have been previously discussed in the literature<sup>17,18</sup>. Almost all processes use fossil carbon sources and are high energy demanding. Managing industry-scale and more eco-friendly production of homogenous and defect-free graphene is one of the main challenges to envisage further commercial use of graphene. The production of graphene-like materials from bioresources (biomass, biowastes...) would open ways for new materials with outstanding properties. This approach, as opposed to the standard graphene manufacturing techniques using chemicals and various solvents, would lower the environmental impact of graphene-like materials synthesis.

<sup>1</sup>Université de Toulouse, Mines Albi, CNRS, Centre RAPSODEE, Campus Jarlard, Route de Teillet, 81013 Albi Cedex 09, France. <sup>2</sup>School of Engineering and Applied Science, Princeton University, Princeton, NJ 08544, USA. <sup>3</sup>Andlinger Center for Energy and the Environment, Princeton University, Princeton, NJ 08544, USA. ✉email: ange.nzihou@mines-albi.fr; ange.nzihou@princeton.edu

Cellulose is a renewable resource and the most abundant organic polymer on Earth. Cellulose is used all over the world for paper production and is widely accessible at cheap cost. Its structure is also relatively homogenous among lignocellulosic biomass, compared to lignin or hemicellulose. The main approach for graphene-like materials synthesis from biomass is pyrolysis to generate graphenic-like biochars. Cellulose is composed of a long chain of D-glucose molecules, with exclusively  $sp^3$  carbons. During cellulose pyrolysis,  $sp^3$  carbons follow multiple and complex chemical rearrangement to be converted into  $sp^2$  carbons and form aromatics rings<sup>19</sup>. Because of this, cellulose is not a favorable material for graphitization.

The graphitization of biomass has been previously investigated in the literature. Graphenic materials were previously obtained from a wide range of biomass, such as woody biomass<sup>20–23</sup>, agricultural<sup>24–35</sup> or food wastes<sup>36,37</sup>, insects<sup>36,38,39</sup> or sewage sludges<sup>37,40</sup>. These studies showed a poor organization of the graphenic materials even with high temperatures treatments ( $> 2000\text{ }^{\circ}\text{C}$ ).

The use of high temperatures implies a significant energetic cost which limits the industrial development of graphene derived from biomass.

Catalytic graphitization was extensively investigated in the past for the production of graphene-like materials from carbon black<sup>41</sup>. A wide range of mineral species was investigated. Transition metals, especially iron and nickel, were considered as the most promising catalysts for their lower cost and great catalytic power<sup>42–47</sup>.

However, only few research addressed the catalytic graphitization of biomass. Calcium is the fifth most widespread minerals in the world and is inherently abundant in lignocellulosic biomass<sup>48–50</sup>. Calcium is cheap, non-toxic and more environmental-friendly than standard catalysts for graphitization. Alkali (Na, K) and alkaline earth metal (Ca, Mg) are known to be promoters for the pyrogasification of biomass while producing the biochar<sup>51–53</sup>. These metals and transition metals like iron and nickel have demonstrated their impact of the structuration of the carbon structure in biochar. Calcium was previously reported to catalyze the graphitization of charcoal<sup>54,55</sup>. The metal catalyzed graphitization mechanism has been explained in the literature<sup>56–58</sup>. The work mostly referred to iron and to nickel to a lesser extent. It is suggested that both particle size and degree of reduction of the iron catalyst positively impact biochar graphitization. In particular, facets of metal catalyst in reduced form provide regions for and promote the precipitation of graphitic carbon. The metal reduces the barrier for carbon nucleation and makes it easier for graphene sheets to form. High dispersion of calcium in cellulose could be expected thanks to linkage of calcium ions with the carboxyl groups<sup>59</sup>. As such, calcium could possibly be a promising catalyst for the graphitization of cellulose biochar and, by extension, of lignocellulosic biomass.

This study focuses on the effect of Ca-loaded for the efficient graphitization of the resulting biochar. For this purpose, commercial cellulose was impregnated with calcium nitrate prior to pyrolysis at  $1800\text{ }^{\circ}\text{C}$ . For clarity reasons, the terms *structure*, *texture* and *nanotexture* will be used as defined by Monthieux et al.<sup>60</sup>. The carbon structure is amorphous, turbostratic or crystalline; the texture defines the organization of the graphene sheets (concentric, aligned...) while the nanotexture describes the length and the stacking of the graphene sheets in the crystal coherence domains.

The carbon organization in the resulting biochar was characterized at a macroscopic (with X-Ray Diffraction, XRD), local (with Raman spectroscopy) and nanoscopic scales (with High-Resolution Transmission Electron Microscopy, HRTEM). XRD provides a general description of the various carbon structures (amorphous, turbostratic, graphene-like) in the samples and estimations of the crystallite sizes. Raman spectroscopy informs about the level of amorphousness and defectiveness of the graphenic structures at the surface of a char particle. HRTEM complements XRD and Raman spectroscopy by investigating at nanoscale the graphenic structures. The results from each characterization technique were further exploited to extract quantitative information about the graphenic structures. Especially, the HRTEM images were processed through a home-made image analysis numerical tool to estimate the crystallite sizes. The combination of experimental methods such as XRD, Raman spectroscopy and HRTEM together with the numerical processing of the data have enable to provide new insights on the mechanism driving the calcium-catalyzed cellulose graphitization.

## Materials and methods

**Biochars origin and preparation.** Biochars, named Ca-1 to Ca-8, were produced by pyrolysis of calcium-impregnated microcrystalline cellulose (Sigma Aldrich CAS: 9004-34-6) under  $\text{N}_2$  at  $1800\text{ }^{\circ}\text{C}$ . The impregnation was conducted by immersion, for 6 h, of 40 g of cellulose in 200 mL of deionized water with dissolved calcium nitrate under agitation. The impregnated cellulose is then filtered and dried. A respective mass of 3, 6, 12, 15, 18, 25 and 40 g of calcium nitrate were dissolved for the preparation of the Ca-1 to Ca-7 samples, the sample Ca-8 was obtained with 40 g of calcium nitrate but with a shorter filtration time than Ca-7. The impregnated cellulose was pyrolyzed at  $800\text{ }^{\circ}\text{C}$  during 1 h under  $\text{N}_2$  with a heating ramp of  $2\text{ }^{\circ}\text{C min}^{-1}$  and a gas flow of  $1\text{ L min}^{-1}$  in a vertical tubular oven (Carbolite tubular furnace). The resulting biochar was then collected and heated up to  $1800\text{ }^{\circ}\text{C}$  (1 h plateau) under  $\text{N}_2$  with a heating ramp of  $2\text{ }^{\circ}\text{C min}^{-1}$  and a gas flow rate of  $300\text{ L min}^{-1}$  in a tubular furnace (Nabertherm RHTH 80/300/18). A commercial graphite (ChemPur CAS: 7782-42-5) was also studied as a reference of highly organized carbon.

The calcium concentration in the impregnated sample (before pyrolysis) was determined by Inductively Coupled Plasma Optical Emission Spectrometry (ICP-OES, Horiba Ultima 2) and defined as follows:

$$\% \text{Ca (wt.\%)} = \frac{m_{\text{Ca}}}{m_{\text{Cellulose}} + m_{\text{Ca}}} \quad (1)$$

The calcium concentrations of the samples are summarized in Table 1.

**Study of the graphitization of biochars.** *X-ray diffraction.* The macro and nanotexture of the graphenic structures in the samples was studied by X-Ray Diffraction (XRD, PANalytical X'pert Pro MPD) with a

Sample	Non-impregnated	Ca-1	Ca-2	Ca-3	Ca-4	Ca-5	Ca-6	Ca-7	Ca-8
%Ca (wt.%)	<0.01	0.32	0.95	1.37	2.12	2.83	3.14	3.83	4.39

**Table 1.** Calcium concentration in the samples.

Cu-K $\alpha$  radiation source ( $\lambda = 1.542 \text{ \AA}$ ), operating at 45 kV and 40 mA. Diffraction peaks were recorded at  $0.5^\circ\text{s}^{-1}$  in the range  $10^\circ$ – $100^\circ$  in  $2\theta$ . The asymmetric  $002$  diffraction peak ( $2\theta \approx 24^\circ$ ) of the biochars was fitted with two pseudo-Voigt functions. The symmetric  $002$  diffraction peak of graphite was fitted with a single pseudo-Voigt. The asymmetric  $10$  ( $2\theta \approx 43^\circ$ ) and  $11$  ( $2\theta \approx 80^\circ$ ) diffraction peaks were both fitted with a Breit–Wigner–Fano function. For the commercial graphite, the  $100$ ,  $101$  and  $110$  diffraction peaks at  $2\theta \approx 42.5^\circ$ ,  $2\theta \approx 44^\circ$  and  $2\theta \approx 78^\circ$  respectively were fitted with a pseudo-Voigt function. The crystallite sizes of the graphenic structures  $L_a$  (in-plane length) and  $L_c$  (stacking height) were determined from the XRD spectra using the Scherrer equation<sup>61</sup>:

$$L(\text{nm}) = \frac{K \cdot \lambda}{\sqrt{\beta^2 - s^2} \cdot \cos\theta} \quad (2)$$

where  $\lambda$  is the radiation wavelength (0.1543 nm),  $K$  is a constant equal to 1.84 and 0.89 for  $L_a$  of the biochars and commercial graphite<sup>62,63</sup> respectively.  $K$  is equal to 0.89 for the determination of  $L_c$  for all samples.  $\beta$  is the Full Width at Half Maximum (FWHM, in rad) of the  $10$  or  $11$  diffraction peaks for  $L_a$  and of the  $002$  peak for  $L_c$ .  $s$  is the FWHM of a standard specimen (silica) to adjust for instrumental broadening.  $\theta$  is the Bragg position of the  $10$  ( $100$  for graphite) and  $002$  diffraction peaks for  $L_a$  and  $L_c$  respectively. The mean value between  $L_a$  determined from the  $10$  and  $11$  peaks was taken. The interlayer spacing  $d_{002}$  was determined using Bragg's law:

$$d_{002}(\text{nm}) = \frac{\lambda}{2 \cdot \sin\theta_{002}} \quad (3)$$

The average number of stacked graphene fringes  $n_{\text{fringes}}$  in graphenic structures was obtained from  $L_c$  and  $d_{002}$  with:

$$n_{\text{fringes}} = \frac{L_c}{d_{002}} + 1 \quad (4)$$

**Raman spectroscopy.** The structure and nanotexture of the samples were studied using Raman spectroscopy (WITec Alpha 300R, laser excitation = 532 nm). The analyses were performed with KBr/biochar pellets (weight ratio biochar/KBr = 0.025). Raman spectra were acquired by studying a  $7 \mu\text{m}$  square (42 acquisitions/line, 42 lines/sample) on the surface of a sample particle. When relevant, the spectra acquisition was refined with the cluster option to obtain a spatial distribution of the various chemical signatures. The D and G bands (at  $1350 \text{ cm}^{-1}$  and  $1680 \text{ cm}^{-1}$  respectively) were both fitted with a Lorentzian function. The crystallites size  $L_a$  was estimated from the Raman results with the Tuinstra and Koenig formula<sup>64</sup>.

$$L_a(\text{nm}) = \frac{4.4}{I_D} \cdot \left( \frac{2.41}{E_L} \right)^\alpha \quad (5)$$

where  $E_L$  is the laser energy (2.3308 eV) and  $I$  the intensity of the D and G bands.  $\alpha$  is a unique coefficient for each sample to account for the laser dependency. The precise determination of  $\alpha$  was not possible. As such,  $\alpha$  was taken as 4 in this study, which correspond to the  $\alpha$  value obtained for ordered graphite. Since the laser energy used in this study (2.3308 eV) is close to the energy used by Tuinstra and Koenig for their formula (2.41 eV), this will limit the influence of  $\alpha$  on  $L_a$  estimation and will not impact the approximate size and variation tendency of  $L_a$ .

**High-resolution transmission electron microscopy.** The structure, texture and nanotexture of the samples were examined at a nanoscopic scale using High-Resolution Transmission Electron Microscopy (HRTEM, JEOL cold-FEG JEM-ARM200F) operated at 200 kV equipped with a probe Cs corrector reaching a spatial resolution of 0.078 nm. HRTEM images were processed using a home-made image analysis numerical tool to obtain quantitative information about the graphene fringes. The algorithm of the tool was adapted from the method described by Yehliu et al.<sup>65</sup>. The main steps of the algorithm are: Selection of regions of interest—Contrast improvement—Image filtering using the Fourier transform—Binarization—Skeletonization—Correction of errors—Calculation of chosen parameters. The tool was implemented in MATLAB software. The contrast of the entry image is first improved by black and white inversion and histogram equalization to better separate the fringes from the background. The image is then converted into the frequency domain with a fast Fourier transform and filtered with a gaussian lowpass filter. The cutoff frequency was selected as  $3.333 \text{ nm}^{-1}$  ( $0.300 \text{ nm}$ )<sup>-1</sup>, meaning that objects separated by less than 0.300 nm are attenuated. As the interlayer spacing in a graphenic structure is usually greater than 0.3354 nm ( $d_{002}$  of hexagonal graphite), no fringes information is lost. A top-hat transformation is then applied to highlight high contrasted areas by correcting nonuniform illumination. The structural element for the top-hat transformation was a disk with an adjustable diameter larger than the apparent thickness of a single fringe to ensure the conservation of the fringes. The image is then binarized with a threshold determined using Otsu's method and skeletonized with MATLAB built-in skeletonization algorithm. Finally, a home-made

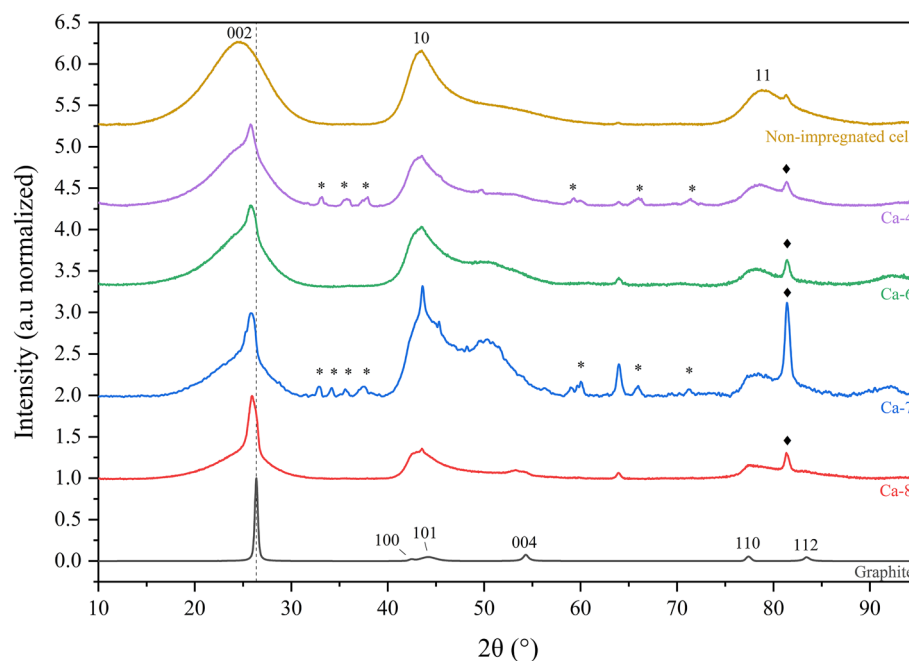


**Figure 1.** XRD patterns ( $\lambda = 1.542 \text{ \AA}$ ) of non-impregnated, Ca-4, Ca-6, Ca-7, Ca-8 samples and commercial graphite. The peak label (asterisk) belongs to the Ca species. The peak label (closed diamond) belongs to the sample holder.

algorithm is applied to correct Y or X fringe ends and aligned fringes separated by less than 0.492 nm (two aromatic rings) are reconnected. The fringes shorter than 0.492 nm are too short to have a physical meaning and are removed.

The numerical tool measures the average crystallite size  $L_a$ , the average fringes tortuosity (defined as the ratio of  $L_a$  on the shortest distance between the fringe extremities), the average interlayer spacing  $d_{002}$  and the number of graphene fringes stacked in a graphenic structure. With this numerical tool, a quantitative comparison of the HRTEM images analysis with the XRD and Raman spectroscopy results can be made.

## Results and discussion

**Investigation of the carbon crystalline organization.** XRD provides insights on the average organization of the carbon matter in the samples. XRD patterns of the non-impregnated biochar and Ca-loaded biochars were acquired after graphitization and compared to a commercial graphite. Only the XRD patterns of the non-impregnated, Ca-4 (%Ca = 2.12 wt.%), Ca-7 (%Ca = 3.83 wt.%), Ca-8 (%Ca = 4.39 wt.%) and commercial graphite samples are presented in Fig. 1. The overall shape of the biochar patterns confirmed the production of carbonaceous turbostratic structures<sup>66</sup> (structures with irregular stacking of the graphene fringes) and the presence of Ca mineral species (peaks label \*) for the impregnated samples. Indeed, non-impregnated and impregnated samples exhibited a broad and asymmetric peak at the 002 and 10 positions while graphite exhibited a sharp and intense 002 peak and a clear distinction between the 101 and 110 peaks. The large broadness of the peaks indicated materials with small crystallite sizes (short-order organization of the graphenic structures) or high curvature of the graphene fringes, as XRD requires flatness of the crystalline structures. This results is known for hard carbon<sup>66</sup>. The 10 and 11 peaks of the non-impregnated and impregnated samples did not differ greatly. The 002 peak position and profile changed significantly with impregnation. The 002 peak shifted from  $2\theta = 24.65^\circ$  for the non-impregnated biochar to  $2\theta = 25.99^\circ$  for Ca-8. This shows a decrease in the interlayer spacing  $d_{002}$  to a value closer to the one for graphite ( $2\theta = 26.37^\circ$ ), which is taken as reference material. The tip of the 002 peak became sharper and a shoulder appeared on its left-side after impregnation. This asymmetry was previously reported for materials with heterogenous carbon structures<sup>67–72</sup>. The left-side of the 002 peak was attributed to poorly organized graphenic structures (randomly oriented texture and weak nanotexture) as found in hard carbons. The sharp tip of the 002 peak of the impregnated samples was attributed to highly organized graphenic structures (aligned texture, large nanotexture and graphene-like structure) as observed in graphitizable carbon or graphite.

To highlight the different carbon structures in the biochars, the 002 peak was fitted with two pseudo-Voigt functions. The left-side referred to Lower-Organized Region (LOR) while the right-side indicated Higher-Organized Region (HOR) as shown in Fig. 2a.  $L_c$  (Eq. 2) and  $d_{002}$  (Eq. 3) were determined for both regions and are presented in Fig. 2b and c versus the initial calcium concentration.

LOR  $d_{002}$  decreased significantly, from 0.466 nm for the non-impregnated sample to a stable value around 0.369 nm for an initial calcium concentration superior to 2 wt.%. This value was slightly higher than the HOR  $d_{002}$  of the non-impregnated sample ( $d_{002} = 0.361 \text{ nm}$ ). HOR  $d_{002}$  showed the same profile, with an initial decrease to

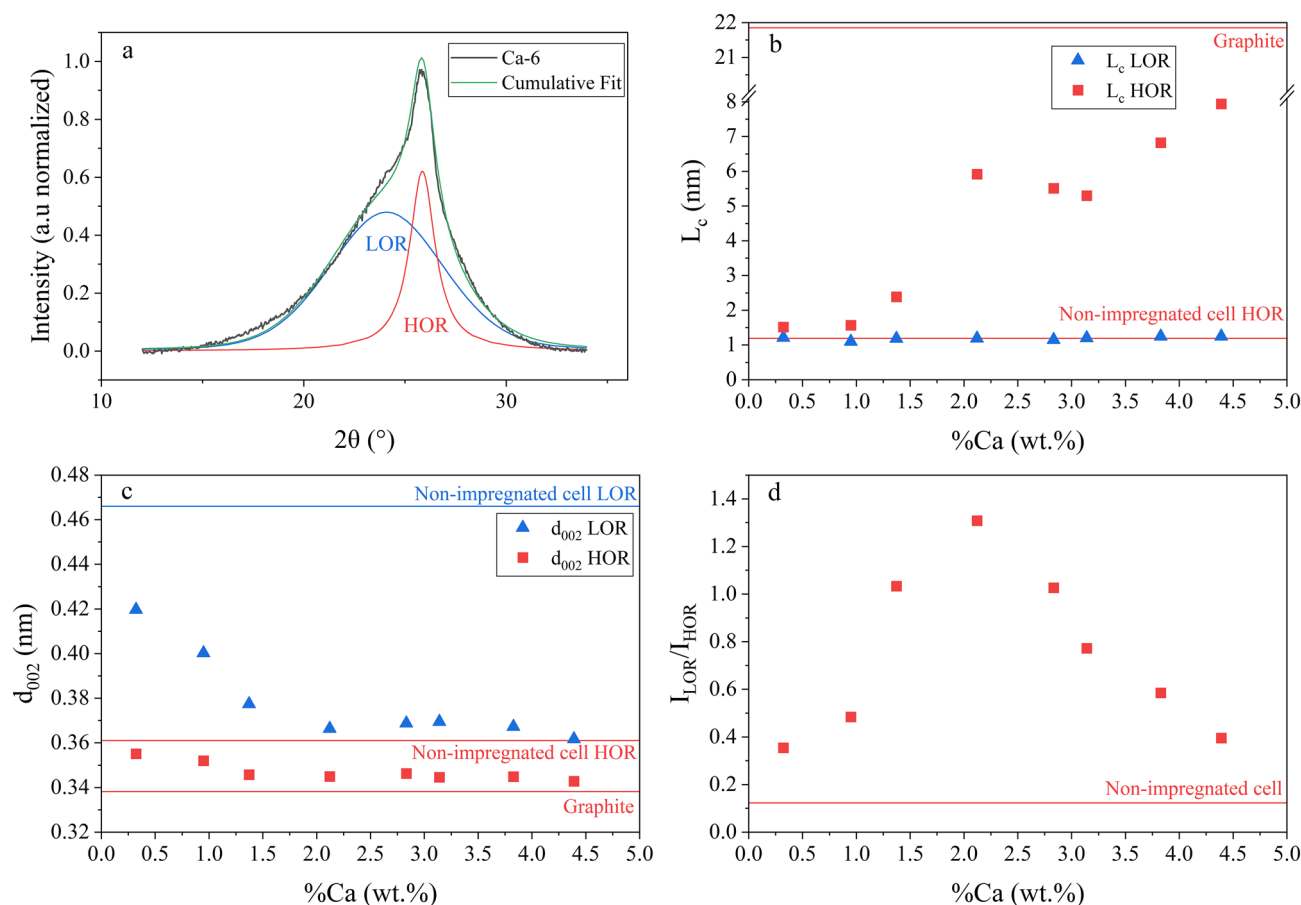


**Figure 2.** (a) Deconvolution of the XRD 002 peak of Ca-6 samples. (b)  $L_c$  of LOR and HOR as a function of %Ca. (c)  $d_{002}$  of LOR and HOR as a function of %Ca. (d)  $I_{LOR}/I_{HOR}$  as a function of %Ca.

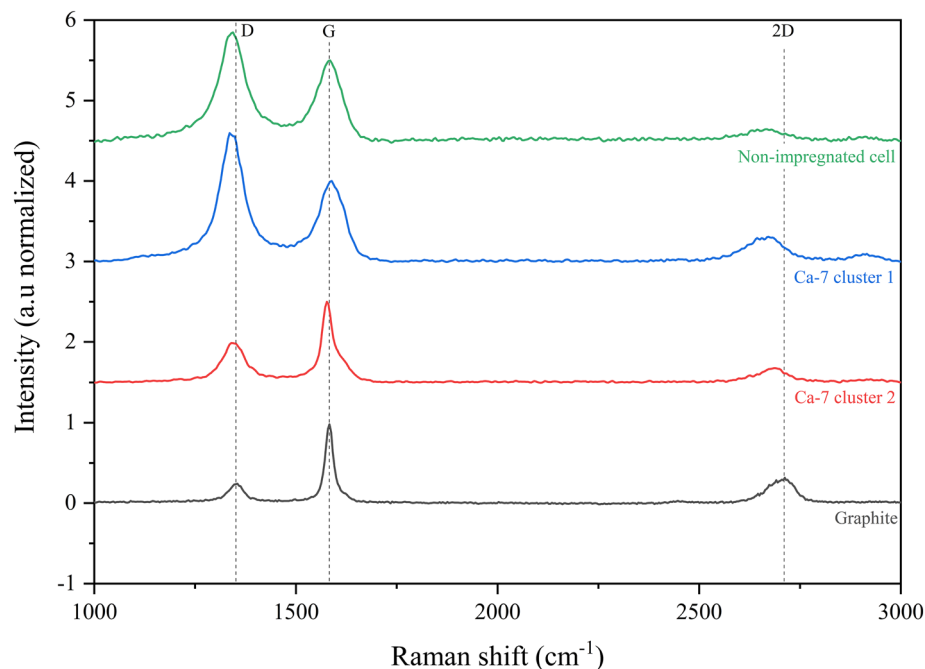
a stable value of 0.345 nm, close to that of the commercial graphite ( $d_{002} = 0.338$  nm). Figure 2b shows LOR and HOR  $L_c$  versus Ca concentration. LOR  $L_c$  remained stable over the calcium concentration at the non-impregnated sample value ( $L_c = 1.24$  nm). At the opposite, HOR  $L_c$  value increased for an initial calcium concentration below 2 wt.% and reached a plateau around 6 nm at an initial calcium concentration between 2 and 3 wt.%, then increased up to 8 nm at higher initial calcium concentrations. The average number of stacked graphene fringes ( $n_{\text{fringes}}$ ) increased from  $\approx 4$  fringes for the non-impregnated sample to  $\approx 24$  fringes for Ca-8 sample, meaning that calcium acted as a catalyst for cellulose graphitization in enhancing the graphenic structure rate.

Figure 2d shows the ratio between LOR and HOR peak intensities ( $I_{LOR}/I_{HOR}$ ). It increased up to  $\approx 2$  wt.% of calcium and then decreased. This profile was unexpected since the HOR domain (and its peak intensity) would likely increase with Ca concentration, leading to a decrease of  $I_{LOR}/I_{HOR}$ . Indeed, highly organized graphenic structures developed with increasing calcium concentration, as it is confirmed by the high HOR  $L_c$  and low HOR  $d_{002}$  values for an initial calcium concentration superior to 2 wt.%. A possible explanation is a variation in the significance of the LOR and HOR peaks among the sample. For the non-impregnated sample, the 002 peak was mainly defined by the HOR peak (low  $I_{LOR}/I_{HOR}$ ). The HOR peak corresponds to poorly organized graphenic structures (high  $d_{002}$  and small  $L_c$ ) as it was observed for hard carbon<sup>73</sup>, whereas the LOR peak was attributed to a small fraction of highly disorganized (amorphous) carbon structures<sup>72</sup>. With calcium impregnation, the disorganized carbon structures rate decreased in favor of much more organized graphene-like structures. For an initial calcium concentration below 2 wt.%, HOR peak mainly composed the 002 peak but the material exhibited a low  $L_c$  value (Fig. 2b) and a high  $d_{002}$  (Fig. 2c). In this stage, the HOR peak represented graphene-like structures with some poorly organized graphenic structures<sup>71</sup>. For initial calcium concentrations above 2 wt.%, the HOR peak represents exclusively graphene-like structures (low  $d_{002}$  and high  $L_c$ ) that mainly referred to regions of the biochar in contact with the calcium particles, while the LOR peak represents hard carbon structures, resulting from free or less contact regions with the catalyst during the heat treatment. In this stage, HOR  $d_{002}$  and  $L_c$  did not vary significantly but  $I_{LOR}/I_{HOR}$  decreased. This could be attributed to a promoting effect of calcium in the conversion of LOR to HOR.

Therefore, additional calcium did not modify further the nanotexture of the graphenic structures but improved the rate of highly organized graphenic structures in the biochar.

Finally, the bulk structure was almost turbostratic and became more graphenic with calcium impregnation, which is confirmed by the quantified nanotextural parameters  $L_c$  (stacking), and  $d_{002}$ . To better understand how the transformation occurred, we have also investigated the carbon organization at local scale.





**Figure 3.** Raman spectra of non-impregnated cell, Ca-7 and commercial graphite samples.

**Investigation of the carbon organization at local scale.** At local scale, Raman spectroscopy gives chemical signature of the samples and can also highlight heterogeneity in chemical compositions. Only the non-impregnated cellulose biochar, Ca-7 and commercial graphite spectra are presented in Fig. 3. Raman spectra of Ca-4 and Ca-6 samples are provided in Supplementary material on Fig. S1. The spectrum of the non-impregnated cellulose biochar had a broad and intense D and G band ( $I_D/I_G = 1.34$ ) whereas the commercial graphite had a small D band and a narrow G band ( $I_D/I_G = 0.23$ ). G band refers to graphenic signature and the D band is likely attributed to defects in the graphene-like materials<sup>74,75</sup>. The defects include, with various intensities, edges, curvature or vacancies among others<sup>74</sup>. Graphite, which is composed of long-ordered graphenic arrangement has a weak D band compared to the G band. For all samples, the D and G bands were clearly separated, which indicated the absence of amorphous carbon through the valley between both bands<sup>76,77</sup>. For each impregnated samples, different chemical signatures, called clusters, could be identified. Two clusters of the Ca-7 sample are displayed in Fig. 3. Some clusters are close to the non-impregnated cellulose biochar spectrum (see Ca-7 cluster 1,  $I_D/I_G = 1.40$ ), this could correspond to spatial domains with limited effect of the catalyst. As these domains were highly defective, they could be attributed to the turbostratic structures previously evidenced by XRD. Some clusters showed a decrease and a thinning of the D band (see Ca-7 cluster 2,  $I_D/I_G = 0.59$ ), meaning a reduction of the defects in the graphene fringes and more organized graphenic structures. The second order bands were observed for all samples, due to the increased organization. The 2D band (double resonance of the D band) gives information on the texture and nanotexture of the graphenic structures using its shape, intensity and position<sup>74</sup>. The D band of the non-impregnated cellulose sample ( $1341\text{ cm}^{-1}$ ) was slightly red-shifted from the D band position of the commercial graphite ( $1351\text{ cm}^{-1}$ ). This shift may be due to defects or curvature of the graphene fringes<sup>76</sup>. The D band position of the impregnated samples ranged between the D band positions of the non-impregnated cellulose and commercial graphite samples, which implied a slightly less defective nanotexture. HRTEM images could give insights on the kind of defects (edges/curvature) involved.

The crystallite size  $L_a$  (Eq. 5) was estimated for each cluster and the computed values are presented in Fig. 4a.  $L_a$  values were very heterogenous, however three kind of graphenic structures could be distinguished. For all samples, structures with  $L_a$  ranging between 3 and 6 nm were found (blue squares in Fig. 4a), close to the  $L_a$  determined for the non-impregnated sample ( $L_a = 3.77\text{ nm}$ ). It could correspond to spatial domains with little or no catalyst, leading to graphenic structures with weak nanotexture, as observed in the non-impregnated sample. The second specific feature corresponds to larger graphenic structures, with  $L_a$  values around 9 nm (green triangles in Fig. 4a). The calcium impregnation led to the apparition of graphenic structures with a more developed nanotexture. Finally, structures with  $L_a$  values superior to 16 nm, very close to  $L_a$  of the commercial graphite were observed for the Ca-3 and Ca-8 samples (red circles in Fig. 4a), meaning that calcium can lead to the formation of highly organized graphenic structures. As these structures were not observed for the other samples, this level of organization is only marginal and can be explained by a local accumulation of calcium.

As Raman spectroscopy targets the carbon organization at the surface of the samples, no relation between  $L_a$  and %Ca could be established.

$L_a$  values extracted from the XRD spectra (Eq. 2) are presented in Fig. 4b for comparison. These  $L_a$  values remained around the  $L_a$  value of the non-impregnated sample (3.91 nm).  $L_a$  values from XRD were in accordance

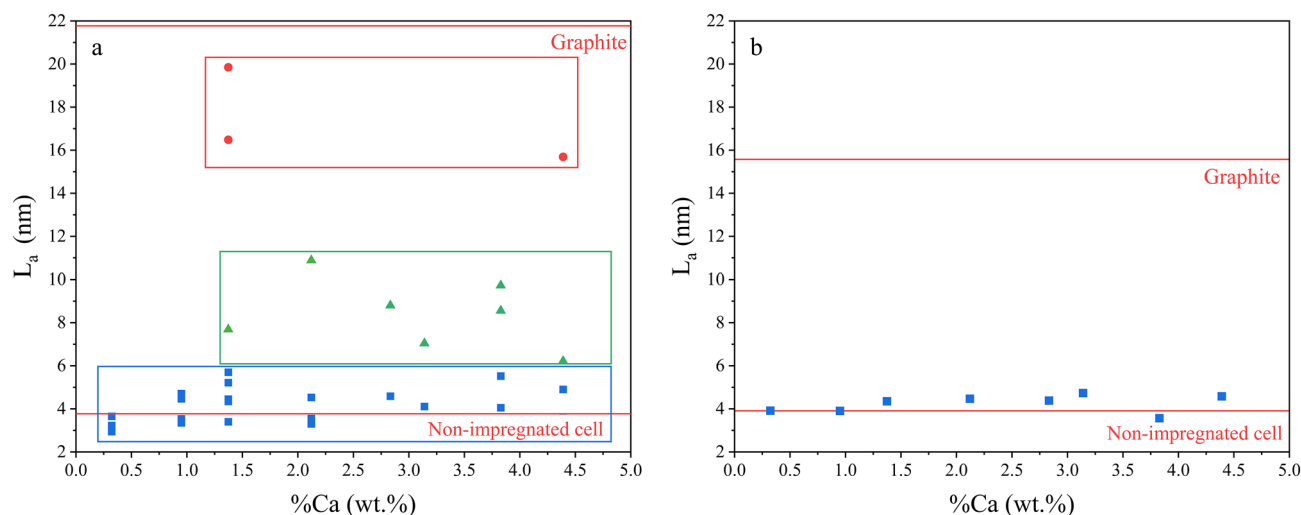


**Figure 4.**  $L_a$  as a function of %Ca from (a) Raman spectroscopy and (b) XRD analysis.

with the smallest  $L_a$  values obtained from Raman analysis, which referred to poorly organized graphenic structures. Since two different graphenic structures (turbostratic and graphene-like) were present in the materials, the contribution to the observed 10 and 11 peaks of the turbostratic structures may have overshadowed those of the graphene-like structures, thus preventing a good estimation of  $L_a$  from XRD.

Raman spectroscopy and XRD both showed a heterogeneity of the carbon structures in the Ca-impregnated samples. XRD indicated the existence of graphenic structures composed of few units of graphene fringes ( $L_c < 2$  nm) stacked with a turbostratic structures ( $d_{002} > 0.361$  nm), similar to the non-impregnated sample. Raman spectroscopy completed this description by indicated a high density of defects ( $I_D/I_G > 1$ ) and poor fringes lengths ( $L_a < 6$  nm) for this kind of graphenic domain. However, XRD informed about the existence of well-developed graphene-like structures ( $L_c \approx 6$  nm,  $d_{002} \approx 0.345$  nm). Raman spectroscopy described them as large ( $L_a > 6$  nm) and low-defective ( $I_D/I_G < 1$ ).

Direct observation of the carbon materials at nanoscopic scale with HRTEM was expected to improve the understanding of the texture and nanotexture of the different carbon structures and complete the observations of the XRD and Raman spectroscopy. Especially, HRTEM should inform about the type of defects encountered in the graphenic structures.

**Nanoscale observation of the carbon organization.** Images obtained from HRTEM enable the direct observation of the inner organization of the materials. HRTEM images were acquired for some samples (non-impregnated cellulose biochar, Ca-2, Ca-4, Ca-6 and Ca-7). Two of the most representative images, obtained from the non-impregnated cellulose biochar and Ca-6 sample, are presented in Fig. 5a and b. Additional images of Ca-4 and Ca-7 samples are available in Supplementary material on Fig. S2.

The image of the non-impregnated cellulose biochar (Fig. 5a) showed highly disorganized graphene fringes, grouped into small graphenic structures long of few nanometers with a poor stacking ( $< 4$  graphene fringes). The graphene fringes were randomly oriented and highly curved, highlighting a weak structuration typical of hard carbons<sup>78</sup>. The strong curvature and short length (implying lot of edges) of the graphene fringes may explain the significant shift of the Raman D band of the non-impregnated cellulose biochar sample from the D band position of graphite, as well as the broad and asymmetric 10 and 11 bands in the XRD spectra. This specific graphene fringes organization was also observed for the impregnated samples.

For the impregnated samples, in addition to poorly organized structures, highly organized graphenic structures were observed (Fig. 5b), characterized by a high structuration and developed nanotexture with large and straight graphene fringes. The observed graphenic structures validated the previous XRD and Raman results and proved the apparition of graphene-like structures promoted by the calcium catalyst.

The disorganization of the graphenic structures in the non-impregnated cellulose biochar prevents a quantitative evaluation of the crystallite sizes of the graphenic structures from the analysis of the HRTEM images alone. That is why a home-made image analysis numerical tool was applied to the HRTEM images to extract some quantitative information about the graphenic structures. For Ca-impregnated samples images, the image analysis tool enables a precise description of each apparent graphene-like structures.

For the Ca-6 sample image, three distinguishable groups of graphene fringes were isolated prior running the tool, named A, B and C. The images obtained after application of the tool are presented in Fig. 5c and d.

Average  $L_a$  and  $d_{002}$  values,  $n_{\text{fringes}}$  and tortuosity value of the graphenic structures were estimated from the HRTEM images and are presented in Table 2. For Ca-6 sample, these values were estimated for each of the three domains and displayed separately in Table 2.

The interlayer spacing  $d_{002}$  computed from the HRTEM image of the non-impregnated cellulose biochar was equal to 0.370 nm, far above the  $d_{002}$  of graphite obtained from XRD ( $d_{002} = 0.338$  nm) but close to the  $d_{002}$  of the hard carbon structures ( $d_{002} = 0.361$  nm) determined from XRD. The average number of graphene fringes stacked  $n_{\text{fringes}}$  in the HRTEM image of the non-impregnated cellulose biochar was equal to 3.3 and the graphene fringes



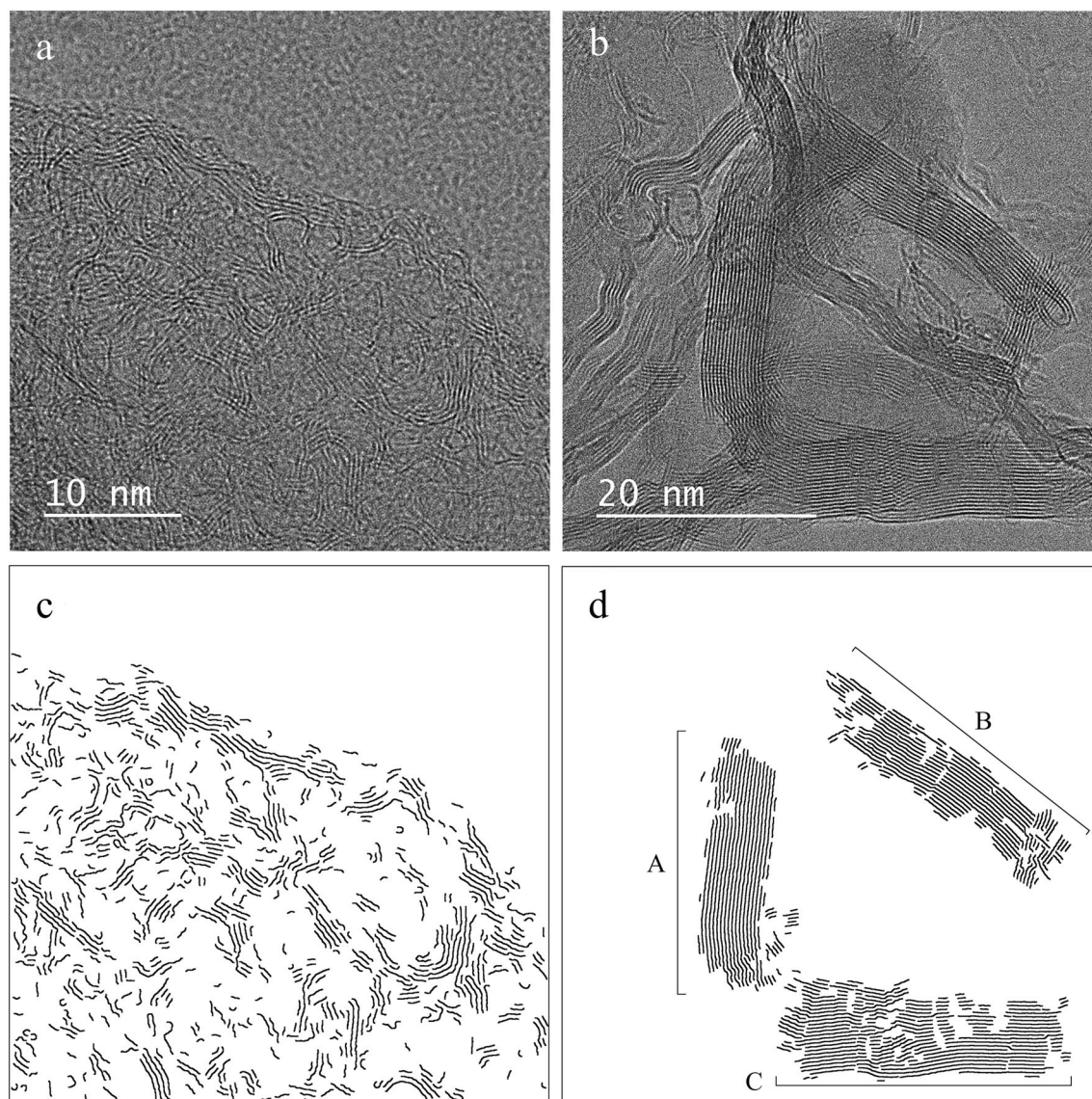


**Figure 5.** (a) HRTEM image of non-impregnated cellulose biochar (X500000). (b) HRTEM image of Ca-6 sample (X400000). (c) Processed image of non-impregnated cellulose biochar. (d) Processed image of Ca-6 sample image.

		$L_a$ (nm)	$d_{002}$ (nm)	$n_{\text{fringes}}$	Tortuosity
Non-impregnated	HRTEM	1.39	0.370	3.3	1.18
Ca-6	HRTEM A	7.87	0.353	18	1.03
	HRTEM B	3.49	0.353	18	1.04
	HRTEM C	3.21	0.348	26	1.02

**Table 2.** Parameters of the graphenic structures from processing of the HRTEM images.

in this sample were also moderately curved (average tortuosity of 1.18). The carbon structures represented in the HRTEM image of the non-impregnated cellulose biochar show a good agreement with the results obtained by XRD and Raman spectroscopy for hard carbon, and highlights their poor organization, with random orientation and defective texture (short and curved fringes).

The three graphenic structures represented in the HRTEM image of the Ca-6 sample had a tortuosity below 1.04, an interlayer spacing  $d_{002}$  below 0.353 nm and a stacking up to 26 fringes. These values were in accordance with the crystallite sizes ( $d_{002} = 0.345$  nm,  $n_{\text{fringes}} \approx 21$ ) computed from XRD for the graphene-like structures. The HRTEM image of Ca-6 sample confirmed the formation of well-organized graphenic structures with calcium impregnation.

$L_a$  obtained from HRTEM images increased from 1.39 nm for the non-impregnated cellulose biochar to 3.21 nm (domain C) and 7.87 nm (domain A) for the Ca-6 sample image. Defects in domains B and C, such as superimpositions and crossings of the graphenic structures, led to fragmentation of the graphene fringes after image processing, explaining the shorter  $L_a$  values obtained for domains B and C compared to domain A. However, all the graphenic structures formed by calcium impregnation were composed of longer graphene fringes than for the non-impregnated cellulose biochar. The  $L_a$  calculated by the numerical tool was lower than the values of  $L_a$  previously reported from XRD and Raman spectroscopy. Only the length of the exposed side of the graphene fringes that are parallel to the direction of observation could be measured from the HRTEM images, whereas XRD and Raman spectroscopy measure the average length of the graphenic structures in the basal plane. As such,  $L_a$  calculated from the HRTEM images cannot be rigorously compared to  $L_a$  calculated from XRD and Raman spectroscopy.

The study of HRTEM images showed that calcium impregnation led to formation of long and straight graphene fringes, gathered in isotropic structures with multiple fringes stacked. All these observations confirmed the XRD and Raman spectroscopy analyses, that suggested the beneficial effect of calcium to form highly organized graphene-like structures at a relatively low temperature.

## Conclusion

Graphitization of cellulose, a poorly organized carbon structure, was achieved after impregnation with calcium, a non-conventional environmental and abundant catalyst. The graphitization was carried out at 1800 °C, below the standard temperature above 2000 °C for thermal synthesis of graphene-like materials. Outstanding investigation of the carbon structures of the samples considered was achieved by studying the biochar organization at macro, micro and nanoscale using X-ray diffraction, Raman spectroscopy and high-resolution transmission electron microscopy paired with an image analysis numerical tool. The results highlighted that calcium promotes the conversion of the hard carbon turbostratic structure into a well-organized and less-defective graphene-like structure.

The graphene-like structures had an in-plane length up to 20 nm and an interlayer spacing of 0.345 nm, near to the crystallite sizes of a standard graphite. An increase of the calcium concentration resulted in a slight improvement of the crystallite sizes of the graphene-like structures but drastically enhanced their rate in the biochar. Further research will focus on the description of the calcium–carbon interactions to better understand the catalytic graphitization mechanism for poorly organized carbon materials such as biomass for further applications.

## Data availability

The datasets generated during and/or analyzed during the current study are available from the corresponding author on reasonable request.

Received: 28 September 2022; Accepted: 7 December 2022

Published online: 13 December 2022

## References

1. Yang, G., Li, L., Lee, W. B. & Ng, M. C. Structure of graphene and its disorders: A review. *Sci. Technol. Adv. Mater.* **19**, 613–648 (2018).
2. Geim, A. K. & Novoselov, K. S. The rise of graphene. *Nat. Mater.* **6**, 183–191 (2007).
3. Mohan, V. B., Lau, K., Hui, D. & Bhattacharyya, D. Graphene-based materials and their composites: A review on production, applications and product limitations. *Compos. Part B Eng.* **142**, 200–220 (2018).
4. Mauter, M. S. & Elimelech, M. Environmental applications of carbon-based nanomaterials. *Environ. Sci. Technol.* **42**, 5843–5859 (2008).
5. Cooper, D. R. *et al.* Experimental review of graphene. *ISRN Condens. Matter Phys.* **2012**, 1–56 (2012).
6. Zhu, Y. *et al.* Graphene and graphene oxide: Synthesis, properties, and applications. *Adv. Mater.* **22**, 3906–3924 (2010).
7. Zhang, Y., Zhang, L. & Zhou, C. Review of chemical vapor deposition of graphene and related applications. *Acc. Chem. Res.* **46**, 2329–2339 (2013).
8. Chung, C. *et al.* Biomedical applications of graphene and graphene oxide. *Acc. Chem. Res.* **46**, 2211–2224 (2013).
9. Shen, H., Zhang, L., Liu, M. & Zhang, Z. Biomedical applications of graphene. *Theranostics* **2**, 283–294 (2012).
10. Chabot, V. *et al.* A review of graphene and graphene oxide sponge: Material synthesis and applications to energy and the environment. *Energy Environ. Sci.* **7**, 1564–1596 (2014).
11. Randviir, E. P., Brownson, D. A. C. & Banks, C. E. A decade of graphene research: Production, applications and outlook. *Mater. Today* **17**, 426–432 (2014).
12. Yan, Y. *et al.* Synthesis of graphene: Potential carbon precursors and approaches. *Nanotechnol. Rev.* **9**, 1284–1314 (2020).
13. Thomas, D.-G., Kavak, E., Hashemi, N., Montazami, R. & Hashemi, N. N. Synthesis of graphene nanosheets through spontaneous sodiation process. *C J. Carbon Res.* **4**, 42 (2018).
14. Choi, W., Lahiri, L., Seelaboyina, R. & Kang, Y. S. Synthesis of graphene and its applications: A review. *Crit. Rev. Solid State Mater. Sci.* **35**, 52–71 (2010).
15. Gadipelli, S. & Guo, Z. X. Graphene-based materials: Synthesis and gas sorption, storage and separation. *Prog. Mater. Sci.* **69**, 1–60 (2015).
16. Ikram, R., Jan, B. M. & Ahmad, W. Advances in synthesis of graphene derivatives using industrial wastes precursors; prospects and challenges. *J. Mater. Res. Technol.* **9**, 15924–15951 (2020).
17. Prekodravac, J. R., Kepic, D. P., Colmenares, J. C., Giannakoudakis, D. A. & Jovanovic, S. P. A comprehensive review on selected graphene synthesis methods: From electrochemical exfoliation through rapid thermal annealing towards biomass pyrolysis. *J. Mater. Chem. C* **9**, 6722–6748 (2021).
18. Lin, L., Peng, H. & Liu, Z. Synthesis challenges for graphene industry. *Nat. Mater.* **18**, 520–524 (2019).
19. Liu, W.-J., Jiang, H. & Yu, H.-Q. Development of biochar-based functional materials: Toward a sustainable platform carbon material. *Chem. Rev.* **115**, 12251–12285 (2015).
20. Severo, L. S. *et al.* Synthesis and Raman characterization of wood sawdust ash, and wood sawdust ash-derived graphene. *Diam. Relat. Mater.* **117**, 108496 (2021).

21. Liu, K.-K. *et al.* Wood-graphene oxide composite for highly efficient solar steam generation and desalination. *ACS Appl. Mater. Interfaces* **9**, 7675–7681 (2017).
22. Ye, R. *et al.* Laser-induced graphene formation on wood. *Adv. Mater.* **29**, 1702211 (2017).
23. Eklhasi, L., Younesi, H., Rashidi, A. & Bahramifar, N. Populus wood biomass-derived graphene for high CO<sub>2</sub> capture at atmospheric pressure and estimated cost of production. *Process Saf. Environ. Prot.* **113**, 97–108 (2018).
24. Yan, Y., Manickam, S., Lester, E., Wu, T. & Pang, C. H. Synthesis of graphene oxide and graphene quantum dots from miscanthus via ultrasound-assisted mechano-chemical cracking method. *Ultrason. Sonochem.* **73**, 105519 (2021).
25. Shams, S. S., Zhang, L. S., Hu, R., Zhang, R. & Zhu, J. Synthesis of graphene from biomass: A green chemistry approach. *Mater. Lett.* **161**, 476–479 (2015).
26. Li, X., Han, C., Chen, X. & Shi, C. Preparation and performance of straw based activated carbon for supercapacitor in non-aqueous electrolytes. *Micropor. Mesopor. Mater.* **131**, 303–309 (2010).
27. Shah, J., Lopez-Mercado, J., Carreon, M. G., Lopez-Miranda, A. & Carreon, M. L. Plasma synthesis of graphene from mango peel. *ACS Omega* **3**, 455–463 (2018).
28. Qin, H. *et al.* Lignin-derived thin-walled graphitic carbon-encapsulated iron nanoparticles: Growth, characterization, and applications. *ACS Sustain. Chem. Eng.* **5**, 1917–1923 (2017).
29. Purkait, T., Singh, G., Singh, M., Kumar, D. & Dey, R. S. Large area few-layer graphene with scalable preparation from waste biomass for high-performance supercapacitor. *Sci. Rep.* **7**, 1–14 (2017).
30. Long, S.-Y. *et al.* Graphene two-dimensional crystal prepared from cellulose two-dimensional crystal hydrolysed from sustainable biomass sugarcane bagasse. *J. Clean. Prod.* **241**, 118209 (2019).
31. Goswami, S., Banerjee, P., Datta, S., Mukhopadhyay, A. & Das, P. Graphene oxide nanoplatelets synthesized with carbonized agro-waste biomass as green precursor and its application for the treatment of dye rich wastewater. *Process Saf. Environ. Prot.* **106**, 163–172 (2017).
32. Sun, L. *et al.* From coconut shell to porous graphene-like nanosheets for high-power supercapacitors. *J. Mater. Chem. A* **1**, 6462–6470 (2013).
33. Perondi, D. *et al.* From cellulose to graphene-like porous carbon nanosheets. *Micropor. Mesopor. Mater.* **323**, 111217 (2021).
34. Debbarma, J., Naik, M. J. P. & Saha, M. From agrowaste to graphene nanosheets: Chemistry and synthesis. *Fuller. Nanotub. Carbon Nanostruct.* **27**, 482–485 (2019).
35. Chen, F., Yang, J., Bai, T., Long, B. & Zhou, X. Facile synthesis of few-layer graphene from biomass waste and its application in lithium ion batteries. *J. Electroanal. Chem.* **768**, 18–26 (2016).
36. Ruan, G., Sun, Z., Peng, Z. & Tour, J. M. Growth of graphene from food, insects, and waste. *ACS Nano* **5**, 7601–7607 (2011).
37. Fang, Z. *et al.* Conversion of biological solid waste to graphene-containing biochar for water remediation: A critical review. *Chem. Eng. J.* **390**, 124611 (2020).
38. Primo, A., Sánchez, E., Delgado, J. M. & García, H. High-yield production of N-doped graphitic platelets by aqueous exfoliation of pyrolyzed chitosan. *Carbon* **68**, 777–783 (2014).
39. Primo, A., Atienzar, P., Sanchez Cortezon, E., Delgado-Sanchez, J.-M. & Garcia, H. From biomass wastes to large-area, high-quality, N-doped graphene: Catalyst-free carbonization of chitosan coatings on arbitrary substrates. *Chem. Commun.* **48**, 9254 (2012).
40. Yin, L., Leng, E., Gong, X., Zhang, Y. & Li, X. Pyrolysis mechanism of  $\beta$ -O-4 type lignin model polymers with different oxygen functional groups on Ca. *J. Anal. Appl. Pyrolysis* **136**, 5569 (2018).
41. Oya, A. & Marsh, H. Phenomena of catalytic graphitization. *J. Mater. Sci.* **17**, 309–322 (1982).
42. Otani, S., Oya, A. & Akagami, J. The effects of nickel on structural development in carbons. *Carbon* **13**, 353–356 (1975).
43. Sevilla, M., Sanchis, C., Valdés-Solis, T., Morallón, E. & Fuertes, A. B. Synthesis of graphitic carbon nanostructures from sawdust and their application as electrocatalyst supports. *J. Phys. Chem. C* **111**, 9749–9756 (2007).
44. Baraniecki, C., Pinchbeck, P. H. & Pickering, F. B. Some aspects of graphitization induced by iron and ferro-silicon additions. *Carbon* **7**, 213–224 (1969).
45. Kiciński, W., Norek, M. & Bystrzejewski, M. Monolithic porous graphitic carbons obtained through catalytic graphitization of carbon xerogels. *J. Phys. Chem. Solids* **74**, 101–109 (2013).
46. Anton, R. In situ TEM investigations of reactions of Ni, Fe and Fe–Ni alloy particles and their oxides with amorphous carbon. *Carbon* **47**, 856–865 (2009).
47. Derbyshire, F. J., Presland, A. E. B. & Trimm, D. L. Graphite formation by the dissolution–precipitation of carbon in cobalt, nickel and iron. *Carbon* **13**, 111–113 (1975).
48. Vassilev, S. V., Baxter, D., Andersen, L. K. & Vassileva, C. G. An overview of the chemical composition of biomass. *Fuel* **89**, 913–933 (2010).
49. Di Blasi, C., Signorelli, G., Di Russo, C. & Rea, G. Product distribution from pyrolysis of wood and agricultural residues. *Ind. Eng. Chem. Res.* **38**, 2216–2224 (1999).
50. Agblevor, F. A., Besler, S. & Wiseloge, A. E. Fast pyrolysis of stored biomass feedstocks. *Energy Fuels* **9**, 635–640 (1995).
51. Nzihou, A., Stanmore, B., Lyczko, N. & Minh, D. P. The catalytic effect of inherent and adsorbed metals on the fast/flash pyrolysis of biomass. *Energy* **170**, 326 (2019).
52. Zhu, C., Maduskar, S., Paulsen, A. D. & Dauenhauer, P. J. Alkaline-earth-metal-catalyzed thin-film pyrolysis of cellulose. *ChemCatChem* **8**, 818–829 (2016).
53. Nzihou, A., Stanmore, B. & Sharrock, P. A review of catalysts for the gasification of biomass char, with some reference to coal. *Energy* **58**, 305–317 (2013).
54. Wang, J., Morishita, K. & Takarada, T. High-temperature interactions between coal char and mixtures of calcium oxide, quartz, and kaolinite. *Energy Fuels* **15**, 1145–1152 (2001).
55. Oya, A., Otani, S. & Tomizuka, I. Letter to the editor: On the structure of turbostratic carbon formed in charcoal by catalytic action of calcium vapor. *Carbon* **17**, 305–306 (1979).
56. Lacroix, L.-M. *et al.* Stable single-crystalline body centered cubic Fe nanoparticles. *Nano Lett.* **11**, 1641–1645 (2011).
57. Fernández-García, M. P. *et al.* Enhanced protection of carbon-encapsulated magnetic nickel nanoparticles through a sucrose-based synthetic strategy. *J. Phys. Chem. C* **115**, 5294–5300 (2011).
58. Ghogia, A., Romero Millán, L. M., White, C. E. & Nzihou, A. Synthesis and growth of green graphene from biochar revealed by magnetic properties of iron catalyst. *ChemSusChem* (2022).
59. Cazorla-Amoros, D. *et al.* Local structure of calcium species dispersed on carbon: Influence of the metal loading procedure and its evolution during pyrolysis. *Energy Fuels* **7**, 625–631 (1993).
60. Monthieux, M. *et al.* Determining the structure of graphene-based flakes from their morphotype. *Carbon* **115**, 128–133 (2017).
61. Lim, D. J., Marks, N. A. & Rowles, M. R. Universal Scherrer equation for graphene fragments. *Carbon* **162**, 475–480 (2020).
62. Warren, B. E. X-Ray diffraction in random layer lattices. *Phys. Rev.* **59**, 693–698 (1941).
63. Klug, H. P. & Alexander, L. E. *X-Ray Diffraction Procedures: For Polycrystalline and Amorphous Materials*, 2nd Edition. (1974).
64. Tuinstra, F. & Koenig, J. L. Raman spectrum of graphite. *J. Chem. Phys.* **53**, 1126–1130 (1970).
65. Yehliu, K., Vander Wal, R. L. & Boehman, A. L. Development of an HRTEM image analysis method to quantify carbon nanostructure. *Combust. Flame* **158**, 1837–1851 (2011).
66. Li, Z. Q., Lu, C. J., Xia, Z. P., Zhou, Y. & Luo, Z. X-ray diffraction patterns of graphite and turbostratic carbon. *Carbon* **45**, 1686–1695 (2007).



67. Lee, S.-M., Lee, S.-H. & Roh, J.-S. Analysis of activation process of carbon black based on structural parameters obtained by XRD analysis. *Crystals* **11**, 153 (2021).
68. Shen, T. D. *et al.* Structural disorder and phase transformation in graphite produced by ball milling. *Nanostruct. Mater.* **7**, 393–399 (1996).
69. Wang, W., Thomas, K. M., Poultney, R. M. & Willmers, R. R. Iron catalysed graphitisation in the blast furnace. *Carbon* **33**, 1525–1535 (1995).
70. Aladekomo, J. B. & Bragg, R. H. Structural transformations induced in graphite by grinding: Analysis of 002 X-ray diffraction line profiles. *Carbon* **28**, 897–906 (1990).
71. Oya, A., Mochizuki, M., Otani, S. & Tomizuka, I. An electron microscopic study on the turbostratic carbon formed in phenolic resin carbon by catalytic action of finely dispersed nickel. *Carbon* **17**, 71–76 (1979).
72. Wu, S., Gu, J., Zhang, X., Wu, Y. & Gao, J. Variation of carbon crystalline structures and CO<sub>2</sub> gasification reactivity of Shenfu coal chars at elevated temperatures. *Energy Fuels* **22**, 199–206 (2008).
73. Mafu, L. D. *et al.* Chemical and structural characterization of char development during lignocellulosic biomass pyrolysis. *Bioresour. Technol.* **243**, 941–948 (2017).
74. Merlen, A., Buijnsters, J. G. & Pardanaud, C. A guide to and review of the use of multiwavelength Raman spectroscopy for characterizing defective aromatic carbon solids: From graphene to amorphous carbons. *Coatings* **7**, 153 (2017).
75. Jin, X. *et al.* Nitrogen and sulfur co-doped hierarchically porous carbon nanotubes for fast potassium ion storage. *Small* **18**, 2203545 (2022).
76. McDonald-Wharry, J., Manley-Harris, M. & Pickering, K. Carbonisation of biomass-derived chars and the thermal reduction of a graphene oxide sample studied using Raman spectroscopy. *Carbon* **59**, 383–405 (2013).
77. Smith, M. W. *et al.* Structural analysis of char by Raman spectroscopy: Improving band assignments through computational calculations from first principles. *Carbon* **100**, 678–692 (2016).
78. Mubari, P. K. *et al.* The X-ray, Raman and TEM signatures of cellulose-derived carbons explained. *C* **8**, 4 (2022).

## Acknowledgements

The authors thank Dr Nathalie Lyczko for assistance with XRD, Laurene Haurie for her help with Raman spectroscopy and Teresa Hungria for the acquisition of the HRTEM images. The graphitization equipment used for this work is supported by the French “Investissements d’Avenir” program under the Laboratory of Excellence, LABEX SOLSTICE, ANR-10-LABX-22-01 grant.

## Author contributions

T.B. wrote the manuscript. E.W.H. and A.N., the supervisors of this work, helped discussing and put the results in a broader perspective. All authors reviewed the manuscript.

## Competing interests

The authors declare no competing interests.

## Additional information

**Supplementary Information** The online version contains supplementary material available at <https://doi.org/10.1038/s41598-022-25943-3>.

**Correspondence** and requests for materials should be addressed to A.N.

**Reprints and permissions information** is available at [www.nature.com/reprints](http://www.nature.com/reprints).

**Publisher’s note** Springer Nature remains neutral with regard to jurisdictional claims in published maps and institutional affiliations.



**Open Access** This article is licensed under a Creative Commons Attribution 4.0 International License, which permits use, sharing, adaptation, distribution and reproduction in any medium or format, as long as you give appropriate credit to the original author(s) and the source, provide a link to the Creative Commons licence, and indicate if changes were made. The images or other third party material in this article are included in the article’s Creative Commons licence, unless indicated otherwise in a credit line to the material. If material is not included in the article’s Creative Commons licence and your intended use is not permitted by statutory regulation or exceeds the permitted use, you will need to obtain permission directly from the copyright holder. To view a copy of this licence, visit <http://creativecommons.org/licenses/by/4.0/>.

© The Author(s) 2022